PAPER

Check for updates

Photoinduced force microscopy as a novel method for the study of microbial nanostructures

Josh Davies-Jones, (ID) *[a] Philip R. Davies, (ID) *[a] Arthur Graf,[a] Dan Hewes,[a] Katja E. Hill (ID) [b] and Michael Pascoe (ID) [a,c]

A detailed comparison of the capabilities of electron microscopy and nano-infrared (IR) microscopy for imaging microbial nanostructures has been carried out for the first time. The surface sensitivity, chemical specificity, and non-destructive nature of spectroscopic mapping is shown to offer significant advantages over transmission electron microscopy (TEM) for the study of biological samples. As well as yielding important topographical information, the distribution of amides, lipids, and carbohydrates across cross-sections of bacterial (*Escherichia coli*, *Staphylococcus aureus*) and fungal (*Candida albicans*) cells was demonstrated using PiFM. The unique information derived from this new mode of spectroscopic mapping of the surface chemistry and biology of microbial cell walls and membranes, may provide new insights into fungal/bacterial cell function as well as having potential use in determining mechanisms of anti-microbial resistance, especially those targeting the cell wall.

Introduction

Antimicrobial resistance (AMR) and the spread of multi-drug resistant microorganisms remains one of the major global health threats facing us today, requiring an in-depth understanding of bacterial and fungal properties at the nanoscale level to try and develop strategies to combat them. Until recently, studying the chemistry of bacteria at this scale presented substantial challenges. A diverse array of analytical tools, each with its unique strengths and limitations, including electron microscopy, optical microscopy, vibrational spectroscopy, and force microscopy techniques can be used to achieve this.[1–5] This paper introduces an emerging technique, photo-induced force microscopy (PiFM), which combines vibrational spectroscopy with nanoscale topography, as a cutting-edge approach to explore the nanoscale chemistry of individual microbial cells and their sub-cellular features.

Vibrational spectroscopy offers the capability of distinguishing between specific biomolecular components which play important roles in a wide range of biological processes, through their characteristic absorption bands in the 900–1900 cm^{-1} "fingerprint" region of the IR spectrum.[6] IR spectroscopy is often combined with optical microscopy to identify the chemistry of physical features *e.g.* the presence of the aromatic amino acid tyrosine in beta sheets,[7,8] which has a characteristic absorption band at about 1655 cm^{-1} due to vibration of the C=O bond in its phenol group.[9–11] Other macromolecules such as lipids, carbohydrates, and nucleic acids can also be identified by IR spectroscopy. For example, the absorption bands at about 2850 cm^{-1} and 2950 cm^{-1} arise from the C–H stretching vibrations of fatty acids and other lipids, while the absorption bands at about 1020 cm^{-1} and 1080 cm^{-1} are often attributed to the C–O–C and C–O stretching vibrations of carbohydrates.[12–14] The value of this chemically-specific information has been recognised for many years.[15–17] However, for optical techniques such as infrared microscopy and confocal Raman microscopy, the diffraction limit of light imposes a maximum resolution of about a μm, thereby preventing the nanoscale imaging necessary to fully characterise biological features.[18,19] Furthermore, infrared spectroscopy typically has penetration depths in biological samples of up to 1 μm, and therefore can only provide information averaged over the "bulk" of a sample rather than surface specific information.[20]

One method to circumvent Abbe's diffraction limit is the use of "near-field" methods based on atomic force microscopy (AFM) which has proven useful in the imaging of the mechanical properties of cells and interactions between cells and their environment.[21] AFM also has the advantage over other techniques such as transmission electron microscopy (TEM) and X-ray photoelectron spectroscopy (XPS), of operating under ambient conditions, with minimal sample preparation

[a] Cardiff Catalysis Institute, Cardiff School of Chemistry, Cardiff University, Cardiff, CF10 3A, UK. E-mail: Daviesja21@cardiff.ac.uk, Daviespr@cardiff.ac.uk, PascoeMJ@cardiff.ac.uk, GrafA2@cardiff.ac.uk, HewesDG@cardiff.ac.uk
[b] Advanced Therapies Group, School of Dentistry, Cardiff University, Cardiff, CF14 4XY, UK. E-mail: Hillke1@cardiff.ac.uk
[c] School of Pharmacy and Pharmaceutical Sciences, Cardiff University, Cardiff, CF10 3BN, UK. E-mail: PascoeMJ@cardiff.ac.uk

needed. What AFM lacks is the chemical specificity needed to understand the distribution of specific molecular components on the sample surface.[22,23]

PiFM bridges the gap between high spatial resolution and chemical specificity by combining the strengths of AFM and vibrational spectroscopy[24] and, as a result, holds immense potential for unveiling the chemistry of cellular surfaces at the nanometre scale. The technique also operates non-destructively, eliminating the need for high-energy electrons or other damaging radiation forms. Additionally, the system functions under ambient conditions rather than the ultra-high vacuums required for electron microscopies.[25] With a lateral resolution of 5 nm and a penetration depth of less than 50 nm, PiFM is uniquely situated to study the nanoscale chemistry of biological samples.[24]

In AFM, one of the natural vibrational resonances (eigenmodes) of a cantilever with a sharp tip, is used to measure the topography of a sample surface, with the spatial resolution primarily dictated by the sharpness of the tip; usually around about 5 nm.[26,27] Advanced techniques like bimodal AFM employ multiple eigenmodes to achieve increased resolution and measure additional properties such as deformation and elastic modulus.[28]

In contrast, in PiFM, the first eigenmode of the tip is used to measure the surface topography of the sample, while the second eigenmode is employed to detect the photoinduced force generated on the tip by oscillations of species on the surface of the sample. Almajhadi et al.[29] demonstrated that the PiFM signal is a result of opto-mechanical damping of the amplitude of the cantilever motion because of the excitation of surface molecules at their vibrational optical resonance.[30,31] Since the molecular excitation is a dipole–dipole based phenomenon, the result is a nanometre resolved vibrational spectroscopy that correlates exactly with dipole–dipole based far-field infrared spectroscopy. PiFM differs from other techniques such as photo-thermal infrared microscopy (PTIR or AFM-IR) and nano-FTIR in that it operates in a non-contact mode, measuring van der Waals forces and interactions without physical contact between the tip and the sample.[30,31]

In contrast, AFM-IR relies on mechanical detection of thermal expansion upon contact, while nano-FTIR uses near-field optics for high-resolution IR spectroscopy. Some of the key aspects of these techniques have been identified in Table 1.

Scattering scanning near-field optical microscopy (s-SNOM) is a technique where light is elastically scattered from a sharp AFM tip and optically detected.[34,35] SNOM has been used successfully in the study of several soft matter materials at the nanoscale, such as cells, bacteria, and viruses.[36–38] While this technique is promising, unlike FM-IR, nano-FTIR and PiFM, it lacks the ability to directly correspond to IR spectroscopy. However, recent applications have seen it successfully paired with IR spectroscopy.[39]

The potential for AFM-IR in imaging individual cells and deciphering the chemistry of microbial samples has recently been demonstrated by Kochan et al.[40,41] They utilised spectral bands from cell wall components to highlight how AFM-IR was able to distinguish between Gram-positive and Gram-negative bacteria, as well as identifying distinct differences in chemical composition between isogenic antibiotic susceptible and resistant *Staphylococccus aureus* strains, with vancomycin intermediate *S. aureus* (VISA) and daptomycin resistant cells shown to possess increased non-intracellular carbohydrates and phospholipid content respectively compared to their susceptible counterparts.[40,41] Although individual bacterial cells were successfully imaged using AFM-IR, its limited resolution hampered its ability to directly investigate the nanoscale features of the cell membrane. Therefore, while these papers represent significant progress in the field of nano vibrational spectroscopy and imaging, there are still critical gaps in the current research.[29] One notable limitation is the under-utilization of the nanoscale resolution of the technique. To date, this aspect (possessed by techniques like TEM) has remained largely unexplored due to the inability of AFM-IR to penetrate the microbial surface. So, an important advantage of PiFM over these applications is its high spectral resolution of 1 cm^{-1}, which can assist in the deconvolution of fine spectral components, which are lost in the 8 cm^{-1} resolution found in AFM-IR in these applications.[40,41]

Table 1 A comparison between the operation modes and resolution of AFM-IR (atomic force microscope-infrared spectroscopy), PiFM and s-SNOM (scattering scanning near-field optical microscopy)

	AFM-IR[32]	PiFM[24,29]	s-SNOM[33]
Operating mode	Operates in contact mode. The sample is illuminated from below with an IR laser *via* total internal reflection. When the wavelength of light matches a material absorbance band, the sample expands. This expansion is detected using the AFM cantilever.	Operates in non-contact mode. It relies on tip–sample force interactions. An excitation laser illuminates the sample surface creating the photo-induced force detected *via* a modulation of the AFM oscillating amplitude.	Based on an apertureless near-field optical microscope design. It utilizes a broadband (white-light) laser source instead of a fixed-wavelength laser.
Spatial resolution	~50–100 nm. This is because the spatial resolution is not determined by the tip radius alone, but also by the thickness of the sample *via* mechanical coupling to surrounding material.	~5–10 nm, Limited by the tip diameter because the tip-enhanced field profile is much smaller than the physical tip profile.	~1–20 nm. The spatial resolution is not determined by the tip radius alone, but also by the thickness of the sample *via* mechanical coupling to surrounding material.
Force detection	Relies on short-range repulsive forces through direct contact.	Background free measurement of attractive van der Waals forces.	Relies on short-range repulsive forces through direct contact.

In the present study, we employed conventional TEM preparation methods to highlight the unique potential of PiFM in imaging biological specimens, while directly comparing it to TEM for the first time. We selected three opportunistic pathogens for the study: *S. aureus* (Gram-positive), *Escherichia coli* (Gram-negative), and *Candida albicans* (yeast), as representative cell types.

Materials and methods

Microbial media and culture conditions

Standard strains of *S. aureus* NCTC 10788, *E. coli* ATCC 10536 and *C. albican*s ATCC 10231 were cultured on tryptone soya agar (E&O Laboratories) for 24 hours at 37 °C (bacteria) or 48 hours at 32 °C (*C. albicans*). Following incubation, isolated colonies were resuspended in sterile tryptone sodium chloride (TSC; 8.5 g L^{-1} NaCl, 1 g L^{-1} tryptone) and dispersed by vortexing with 3 mm glass beads. Using a spectrophotometer, A_{630} was adjusted to 0.5, to yield microbial suspensions of approximately 10^8 colony forming units (CFU) per ml (bacteria) or 10^7 CFU per ml (*C. albicans*).

Fixation and embedding of microbial samples

Samples were fixed by adding 1 part cell suspension to 9 parts fixing solution (2 wt% glutaraldehyde in 0.1 M sodium cacodylate, pH 7.2). After 24 hours, fixed suspensions were centrifuged at 100*g* for 5 minutes. After removal of the supernatant, pellets were resuspended 1 : 1 with 4% (w/v) molten (50 °C) low melting point agarose (ThermoFisher Scientific) in polypropylene microcentrifuge tubes and allowed to cool. The agarose blocks were cut into 1 mm^3 sections and post-fixed in 1% osmium tetroxide for 2 hours. The samples were then washed with distilled water and block stained with uranium acetate (2%) for 2 hours. After washing with distilled water, the blocks were dehydrated in a series of propan-2-ol (50, 70, 90 and 100%) for 15 minutes each. Dehydrated blocks were transferred to 50% TAAB embedding resin (TER; TAAB Laboratories Equipment Ltd) in propan-2-ol for 30 minutes and then transferred to 100% TER for 1 hour, three times. Samples were then embedded in 100% TER at 60 °C for 24 hours in truncated polypropylene moulds (TAAB Laboratories Equipment Ltd). Samples were cut into 100–300 nm thick sections using a diamond knife, collected onto 300 mesh copper grids. Some variations in the thickness of sections can be expected due to differences in physical properties between the resin and biological matter.[42,43]

Transmission electron microscopy (TEM)

For TEM imaging, the sections were subsequently stained with lead citrate and examined in a JEOL 2100 TEM (Jeol ltd, Japan) at 200 kV. Post-acquisition, the images were processed using ImageJ, a public domain program developed by the National Institutes of Health (NIH) to improve image brightness and contrast.

Photoinduced force microscopy (PiFM)

In the PiFM analysis, samples were prepared as unstained sections supported on 300 lines per inch mesh copper grids. Imaging and spectral data were acquired using a Vista One nano-IR microscope & spectrometer (Molecular Vista Inc, USA) equipped with a Bloc 780–1930 cm^{-1} quantum-cascade laser (QCL) and Vistascan Version 28 (Molecular Vista Inc, USA). Non-contact high-resolution PtIr-coated (NCHR) cantilevers were used in the measurements. These cantilevers were initially sourced from Molecular Vista 3.2 release 18 (Molecular Vista Inc, USA) and had a spring constant of 45 N m^{-1} and a resonance frequency of 335 kHz.

All measurements were conducted on three microbial cells per species in sideband mode, providing a 20 nm penetration depth, with a spectral resolution of 1 cm^{-1}. Cells were selected randomly from those whose cytoplasmic membrane and cytoplasm were clearly apparent at the focal plane. Subsequently, both spectra and images were subjected to analysis using Surfaceworks 3.0 Release 32 (Molecular Vista Inc, USA). Further spectral subtractions were carried out using OMNIC (Thermo Fisher Scientific), and data fitting was performed with CasaXPS version 2.3.2428.[44] To gain insights into microbial species differentiation, Principal Component Analysis (PCA) was applied to nine spectra, each derived from an average of 20 repetitions. The spectra were organized into a matrix and subjected to analysis in MATLAB (The MathWorks Inc., 2022, R2022b). The PCA approach in this study was specifically tailored to differentiate microbial species based on their unique spectral features. This approach differs from the PCA technique employed in *e.g.* Otter *et al.* (2023), where the primary objective was to generate component maps.[45] The distinct aim of our study was to underscore the ability of PiFM to discriminate between microbial species through their individual spectral characteristics, rather than mapping their spatial distribution.

Results and discussion

Comparison of FTIR and PiFM spectroscopy

Conventional antibiotic susceptibility testing using antibiogram tests requires 18–24 hours to yield results, due to limits on the rates of bacterial growth within laboratories. Infrared spectroscopy is currently being developed to try to improve these diagnostic times. IR spectroscopy has been successfully used on urine samples from urinary tract infections to detect susceptibility and resistance to extended spectrum β-lactamases (ESBLs), fluoroquinolones and aminoglycosides in a range of bacteria including *E. coli*, *Klebsiella pneumoniae* and *Proteus mirabilis*[46–49] with accuracy levels as high as 89% reported.

A comparison of typical IR spectra of the three different cell types with that recorded by PiFM at a specific point on the surface is shown in Fig. 1. The data shows that there is a broad agreement between the FTIR spectra of organic species at cell surfaces reported in the literature[50–52] and the PiFM data,
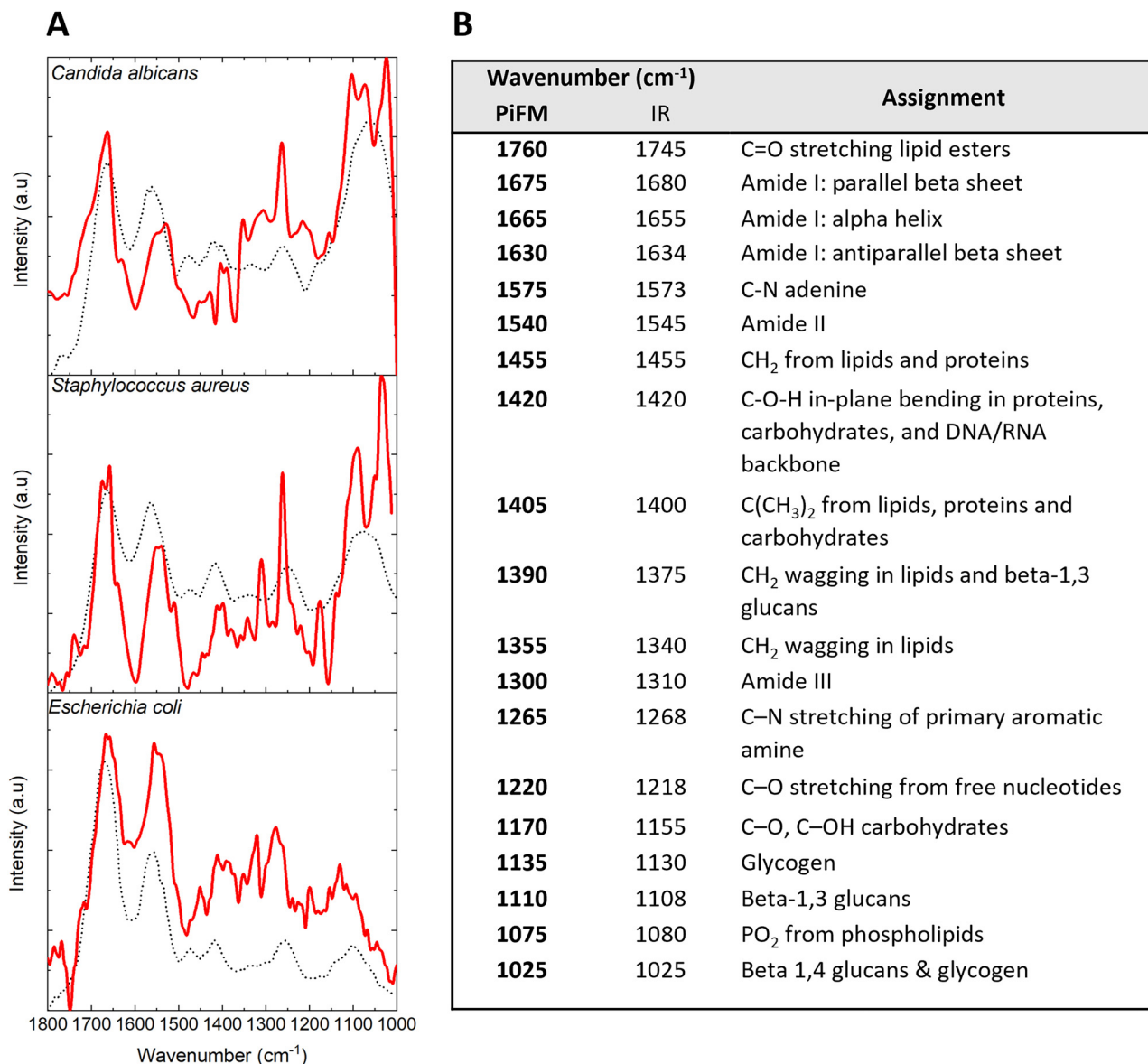
A

B

Wavenumber (cm⁻¹)		Assignment
PiFM	IR	
1760	1745	C=O stretching lipid esters
1675	1680	Amide I: parallel beta sheet
1665	1655	Amide I: alpha helix
1630	1634	Amide I: antiparallel beta sheet
1575	1573	C–N adenine
1540	1545	Amide II
1455	1455	CH_2 from lipids and proteins
1420	1420	C-O-H in-plane bending in proteins, carbohydrates, and DNA/RNA backbone
1405	1400	$C(CH_3)_2$ from lipids, proteins and carbohydrates
1390	1375	CH_2 wagging in lipids and beta-1,3 glucans
1355	1340	CH_2 wagging in lipids
1300	1310	Amide III
1265	1268	C–N stretching of primary aromatic amine
1220	1218	C–O stretching from free nucleotides
1170	1155	C–O, C–OH carbohydrates
1135	1130	Glycogen
1110	1108	Beta-1,3 glucans
1075	1080	PO_2 from phospholipids
1025	1025	Beta 1,4 glucans & glycogen

Fig. 1 (A) Mean PiFM (red line) and FTIR spectra (black dotted line) for *E. coli*, *S. aureus* and *C. albicans* with reference spectra taken from the literature.[50–52] (B) Table comparing PiFM spectra against general FTIR assignments for microbial samples.

although some important differences between the two spectra were observed. For example, PiFM analysis of *C. albicans* revealed a broad signal at 1220 cm⁻¹, which was absent in the reference spectra and corresponds to C–O stretches in free nucleotides. Since these samples were sectioned, it is possible that PiFM may directly assay intracellular contents, producing higher proportions of typical DNA or nucleotide stretches. This effect was seen across all three of the samples tested. Most of the differences observed between FTIR and PiFM were slight shifts in positions, or the presence of additional peaks in the PiFM spectra within areas which previously produced broad signals. One such example occurs in the 1000–1100 cm⁻¹ region of both the *S. aureus* and *C. albicans* spectra, with the PiFM spectra showing 2 peaks where only 1

broad peak was observed within the reference FTIR spectrum, possibly consisting of a combination of the peaks that are separately resolved in the PiFM spectra. The fundamental frequency resolution of PiFM is ~1 cm⁻¹, similar to that of a standard FTIR spectrometer. The better resolution of the PiFM spectra is therefore likely to be due to the high lateral resolution of the PiFM. Depending on the laser frequency, a typical ATR-FTIR system samples an area between 2.5 to 25 μm in diameter, 250 to 2500 times larger than the area sampled by PiFM. Since many bacteria are typically 1 μm or less in length, FTIR spectra therefore reports an average over the entire cell, whereas PiFM provides information on specific points on the cell, and thus is capable of identifying subtle changes in the micro- and nanostructure of the surface.

Comparison between PiFM and TEM imaging of bacterial and yeast cell sections

For a fair comparison between the two imaging methods, we used the same sample preparation method for both TEM and PiFM, embedding the cells in epoxy resin and cutting sections using a microtome. Since PiFM can only measure the spectral signal of compounds present within the first ~200 nm of a sample, sectioning the bacteria was necessary to study their cellular contents, although the cellular surface may also be studied without such intrusive manipulation. The PiFM images in Fig. 2 and 3 were found to match well with previously reported ATR-FTIR fingerprints of the three species.[50,53,54] With a theoretical resolution of 0.2 nm, TEM produced high resolution images of all three species of microbes examined within this study and, was clearly able to

Fig. 2 Comparison of PiFM spectral images with transmission electron micrographs (TEM) of cross-sectioned cell preparations of the three different microbes. In the PiFM images (A, C and E), colours correspond to the intensities of peaks at approximately 1665, 1555 and 1100−1075 cm^{-1}, which are assigned to amide I (red), amide II (green) and carbohydrate/phospholipids (blue) respectively. (A and B) *E. coli*, with arrows identifying (i) nucleoid & cytoplasm, (ii) cytoplasmic membrane, (iii) cell wall, outer membrane & capsule. (C and D) *S. aureus* with arrows identifying (i) cytoplasm, (ii) plasma membrane, (iii) cell wall (iv) septum. (E and F) *C. albicans* with arrows identifying (i) cytoplasm, (ii) plasma membrane, (iii) cell wall, (iv) vacuole, (v) nucleus.
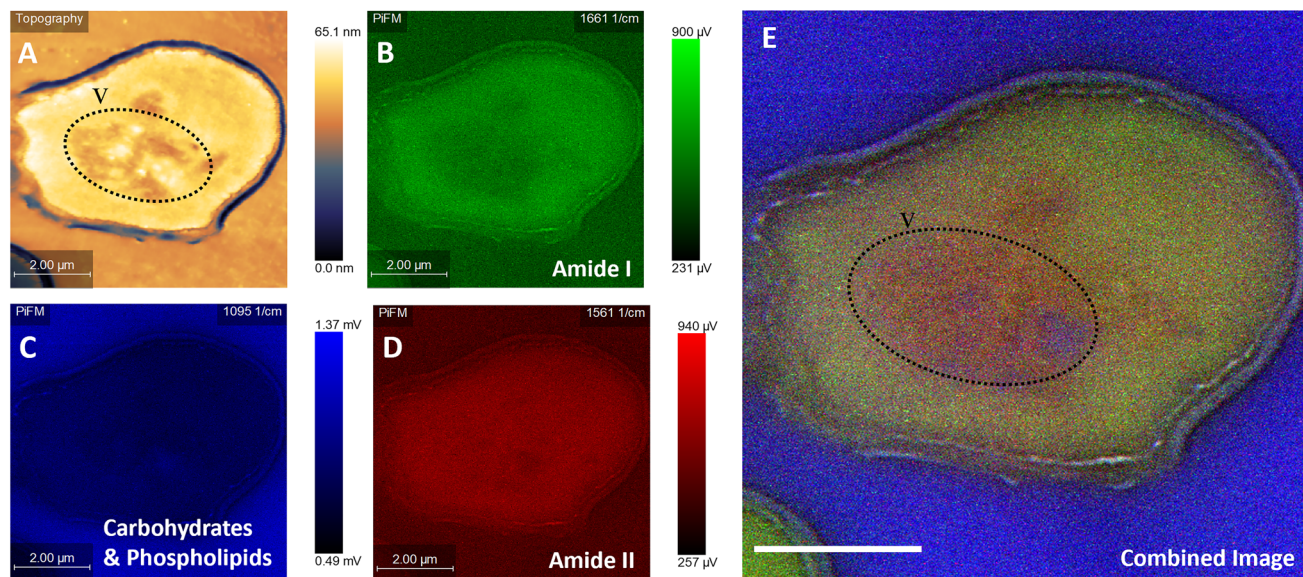
Fig. 3 PiFM micrographs and spectral images of a damaged *C. albicans* cell, the source of the damage is unknown but could be caused through the sectioning procedure. (A) Topographical image, (B) hyperspectral image taken at 1661 cm^{-1}, (C) spectral image taken 1095 cm^{-1}, (D) spectral image taken at 1561 cm^{-1} and (E) combined image of B–D. The vacuole is marked with "V" and damaged areas of the cell wall are highlighted in yellow.

distinguish cellular structures such as the cell wall of *S. aureus* and the vacuole and nucleus of *C. albicans* (Fig. 2).[55] In contrast, the PiFM images have an approximate pixel size of 5 nm, thus providing both spectral and morphological information. Of particular importance, is the ability of PiFM to image the outer membrane of the Gram-negative bacterium *E. coli*, which is mostly composed of extracellular polymers and carbohydrates, and appears as a bright blue halo around the cell (Fig. 2A) which is not distinguishable in the TEM image (Fig. 2B). In *S. aureus*, the cell wall structure is clearly visible in the PiFM images, with the peptidoglycan constituent, comprised of β-(1,4) linked *N*-acetylglucosamine and *N*-acetylmuramic acid, shown as lilac in colour (Fig. 2C) in contrast to the TEM image (Fig. 2D). In addition, when studying *C. albicans* (Fig. 2E), the cell wall is mostly formed of chitin and β (1,3)-glucan and appears as turquoise in colour in the combined image, with the organelles particularly highlighted in the TEM image (Fig. 2F). The background of the PiFM images (which varies between images from blue to lilac) is a consistent signal due to background absorption across the sample resulting from the epoxy resin. This was therefore discounted from our analysis when exploring the relative intensities of each component.

A particular drawback of PiFM is its inability to penetrate through the entire sample, resulting in a less clear differentiation between the cytoplasm and the cellular machinery of *e.g.*, *C. albicans* (Fig. 2). However, this is not always the case as illustrated in Fig. 3, where several organelles can be observed (outlined with a dotted line), perhaps because they are close to the cell surface. Bacteria are simple prokaryotic cells with no nucleus (the nucleoid being an irregularly shaped region

within the cell containing the genetic material), whilst yeasts are eukaryotic, possessing a differentiated nucleus and a variety of other organelles. Vacuoles occupy up to 20% of the *C. albicans* cell and are thought to be involved in many cellular functions which enhance its ability to adapt to stress and changes in host environment during infection, so the ability to image and study these directly is important.[56] The vacuoles are filled with hydrolase enzymes, amino acids, cations and are the main store of polyphosphates within a yeast cell.[57,58]

Fig. 3 illustrates the usefulness of PiFM for the direct study of organelles within the yeast cell, demonstrated by the large area of heterogenous chemistry in the cell centre occupying roughly 25% of the intracellular space, imaged as a drop in topography of ∼20 nm. It is hypothesised that this area of the cell (identified with a dotted line) is a vacuole, which was filled with high ratios of amide II and phosphate contributions (Fig. 3A and E). This matches well with the theoretical content of a vacuole; the blue areas corresponding to polyphosphate stores and the red corresponding to amines (Fig. 3C and D). Surprisingly, a lower amide I contribution was also noted in this area (Fig. 3B). Amino acids such as lysine, glycine and tyrosine are known to adsorb in the 1620 and 1550 cm^{-1} region for amide I and amide II respectively. It could therefore be postulated that these areas may correspond to dissociated states of free amino acids and proteins present within the acidic vacuole of the yeast cell resulting from subtle changes in their bonding, thus reducing the contribution of the amide I peak, or perhaps shifting it to a lower wavenumber than 1660 cm^{-1}.

The cell in Fig. 3 is clearly damaged, with the plasma membrane noticeably pulled away from the cell wall, (seen as the

light blue line running 200 nm parallel to the cell wall). The plasma membrane is a mosaic of phospholipid molecules and indirectly bound proteins.[59,60] In areas where the wall and membrane were damaged, there appears to be a higher proportion of the 1095 cm^{-1} contribution, compared to areas of the cell with a more rounded and intact plasma membrane. In contrast, in areas of greater plasma membrane integrity, larger components of amides I and II were noted. The areas of damage represent a significant shift in phospholipid organisation, resulting in a higher contribution to the 1095 cm^{-1} signal from PO$_4$. Hence, the ability of the PiFM to directly image and characterise the chemistry of different organelles and areas of the cell is a significant advantage over that of TEM, offering label-free imaging and avoiding the need for extraction of cellular contents (Fig. 3E).

Principal component analysis (PCA)

To assess the ability of PiFM to distinguish between different microbial species, we conducted both PCA and hierarchical cluster analyses on the vibrational spectra recorded from the different microbes (Fig. 4). Both analyses showed that the system was effective in differentiating between the three species studied. The dendrogram (Fig. 4A) provides a visual representation of the hierarchical cluster analysis performed on the vibrational spectra of the different microbial species. A dendrogram shows the relationship and similarities between objects or clusters. In this case, it demonstrates the dissimilarity or proximity between the microbial species studied. The "distance" on the x-axis of the dendrogram represents the measure of dissimilarity or proximity between the objects or clusters, successfully illustrating the similarity of vibrational spectra within each microbial species. The linkage function group objects are based on their closest distances, forming clusters, and assigning unique index values to the newly formed clusters. In this dendrogram, the clustering shows that PiFM could effectively distinguish between bacteria and fungi, as well as between Gram-positive and Gram-negative bacterial species. It is important to note that, whilst PCA is a useful technique for demonstrating differences in data sets, further exploration of different species and growth conditions is necessary to fully understand the ability of PiFM to differentiate between microbial species. Factors such as pH, temperature, and culture conditions can all influence the biochemical profile of microorganisms, and individual differences between microbes of the same genera and species should also be considered. Therefore, further analysis and method development is required to validate the effectiveness of the technique for microbial species differentiation.[61]

PCA illustrated a few key areas within the spectra that differed between the three microbial species (Fig. 4B). PC1 was responsible for 53% of the differentiation of the data with particularly interesting differentiation coming in the 1669, 1511, 1225 and 1190 cm^{-1} regions. These correspond to changes in the amide I, amide II, free nucleotides, and carbohydrates respectively, implying that the majority of PC1 arose from changes in the proteins and amino acids present in each

species. PC2 (21%) was mostly characterised by changes in the 1730, 1595, 1425 and 1090 cm^{-1} regions, of which the majority can be attributed to changes in the lipid and phospholipid structures of the microbes. PC3 only corresponded to 12% of the differentiation between the species, but was mostly characterised by peaks in the 1120, 1295, 1400 and 1730 cm^{-1} regions which are only loosely connected. Here, regions 1120 cm^{-1} and 1400 cm^{-1} can be attributed to changes in the structure of polysaccharides such as chitin or glucans, and the peaks at 1295 cm^{-1} and 1730 cm^{-1} probably correspond to changes in the amide III and lipid esters respectively. A mix of contributions characterised by the carbohydrates, proteins and lipids is not surprising since they correspond to a high proportion of the composition of a microbial sample, and with large changes in side-chains, conformation and functionality, it was expected that these biomolecules would be very important for differentiation between the three cell types.[62,63] Although these results are extremely encouraging, comparisons between microbes of the same species have yet to be performed to confirm the validity of the technique, demonstrating that further analysis and method development is still required.
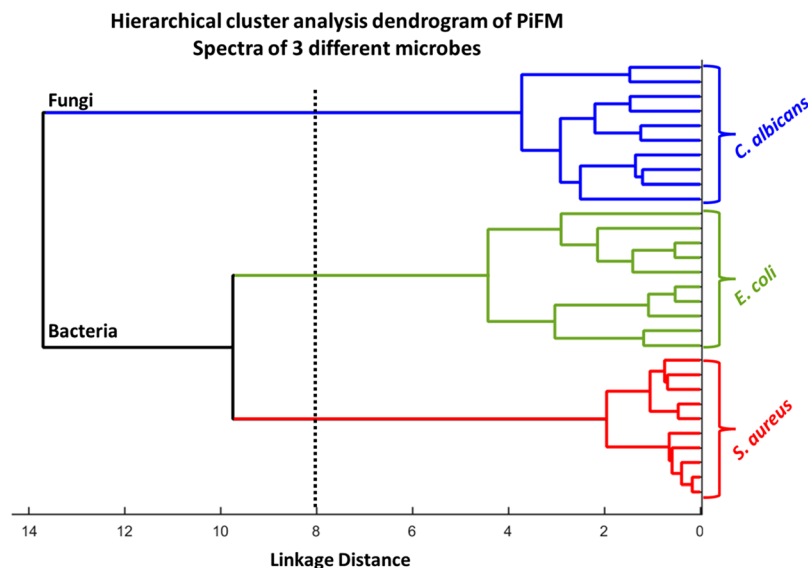
Spectral imaging

The most significant advantage of PiFM for the analysis of microbes is demonstrated by the IR spectral profiles across the different samples tested at a spatial resolution of <20 nm (Fig. 5–7). The cell wall and cytoplasmic membrane of *C. albicans* has been widely studied in recent years, and its structure described as sequential layers of mannoproteins (outer layer) and glucans mixed with chitins (inner layer) followed by a cell membrane mostly constructed from phospholipids.[60,64] PiFM spectra (Fig. 5A–D) were taken at four specific sites of the cell, namely: the outer cell wall, the inner cell wall, the cell membrane, and the cytoplasm (Fig. 5E). However, these spectra did not exhibit the significant differences previously observed in the spectral images. This may be due to the data processing performed to remove peaks corresponding to the epoxy resin, causing a reduction in the sensitivity of the PiFM spectra. Nevertheless, some notable key areas of difference still support the changes seen within the spectral images.

Firstly, positions 3 and 4 at the outer and inner cell wall showed higher absorptions in the 1025, 1095 and 1110 cm^{-1} regions when compared to the amide I region. These correspond to glucan polysaccharides and phospholipids. Position 4 shows a large shoulder at 1735 cm^{-1} corresponding to esters present within the phospholipids. Furthermore, a peak at 1225 cm^{-1} shows increased levels of intensity towards the centre of the cell. This corresponds to free nucleotides present within the cytoplasm for DNA and RNA replication. The last, most notable difference in the PiFM spectra is demonstrated at position 4 (outer cell wall). Here, two components corresponding to the amide II region at 1530 and 1565 cm^{-1} were observed. Region 1530 cm^{-1} displayed a relative increase in intensity compared to region 1565 cm^{-1} when progressing from position 1 to position 4. While the cause of this change
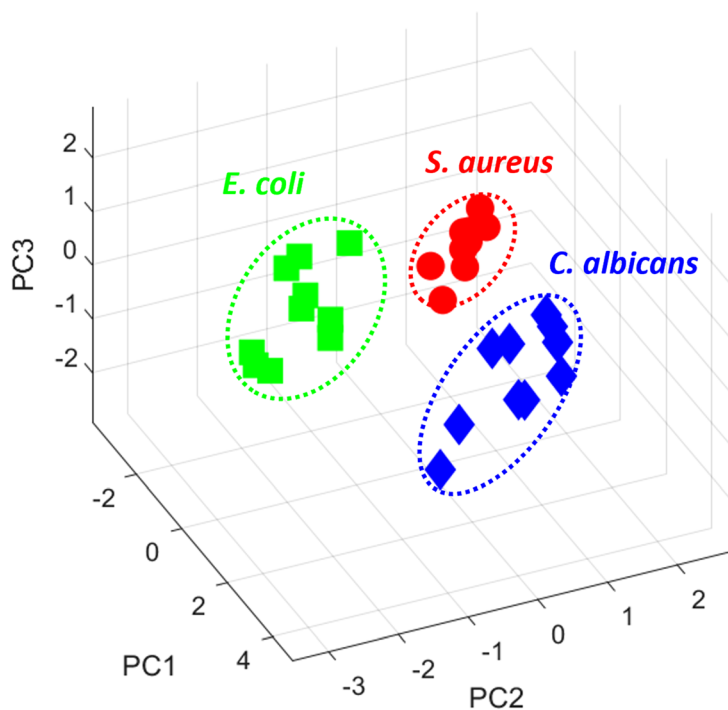
A

B

Fig. 4 (A) Hierarchical cluster plot dendrogram analyses of the vibrational spectra recorded from the different microbes *C. albicans*, *E. coli* and *S. aureus* (*n* = 10). The "distance" on the *x*-axis of a dendrogram represents the measure of dissimilarity or proximity between objects or clusters. (B) Principal component (PC) analysis of the data in A for *C. albicans*, *E. coli* and *S. aureus*. PC1, PC2 and PC3 representing 53%, 21% and 12% of the score respectively.

is not clear, it is likely due to changes in the conformation of the amides and proteins present within the inner and outer cell wall. These differences between different structures can clearly be seen in the combined image (Fig. 5F). The outermost layer of the cell wall is characterised as being rich in glyco-proteins (mannoprotein), (predominantly coloured in red and green) corresponding to the amide I and amide II functional-

ities present in the mannoprotein coating. The next layer (inner cell wall) is mostly comprised of polysaccharides. This can be observed in the ratio between the amide peaks and those of the 1074 cm^{-1} polysaccharide peak, (which mostly corresponds to phosphate within the phospholipids) but will also have contributions from the beta glucans forming the structural component of the cell wall. The next (cell mem-
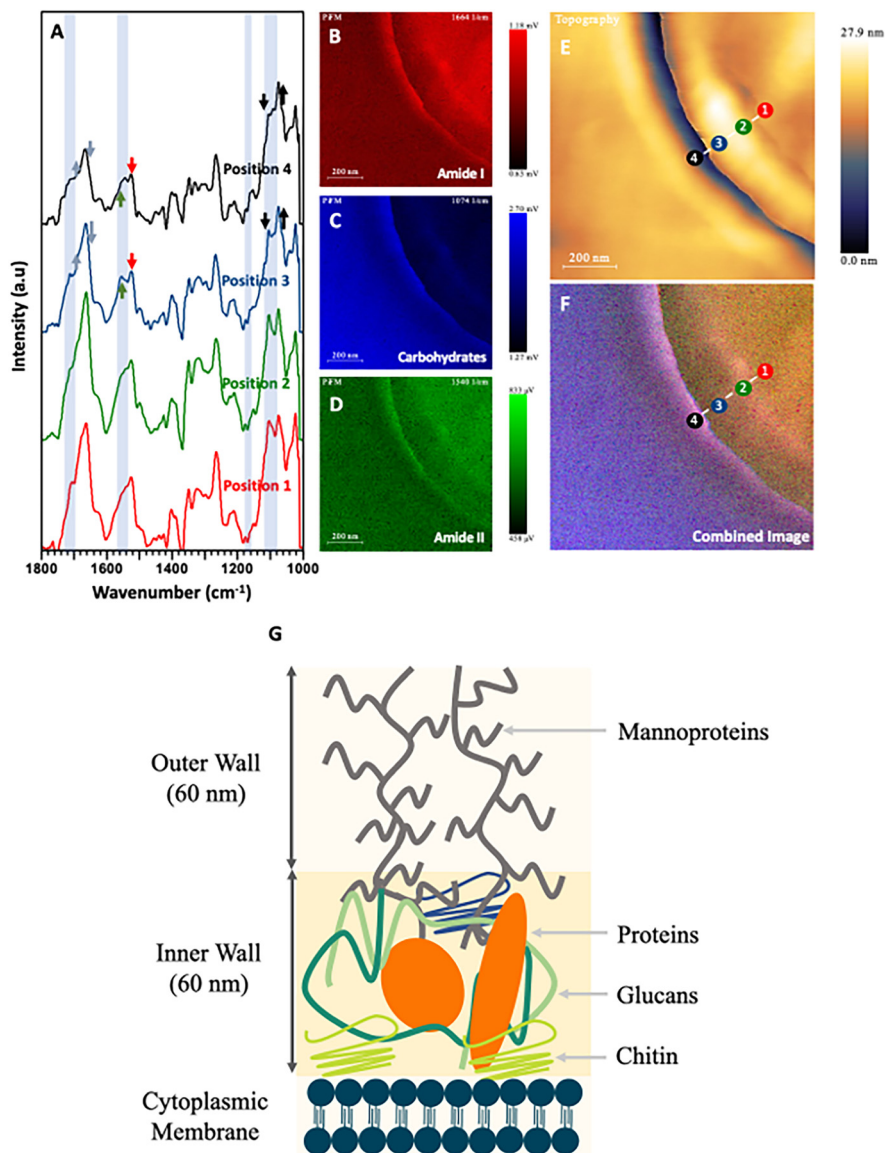
Fig. 5 (A) PiFM spectra taken from four positions (1 to 4) across the cell wall of a sectioned *C. albicans* cell where each position and colour correspond to the indicated position and colour in (E) and (F). (B) Spectral map of 1664 cm^{-1} intensity. (C) Spectral map of 1074 cm^{-1} intensity. (D) Spectral map of 1540 cm^{-1} intensity. (E) Topographical map of *C. albicans* across the cell wall. (F) Combined image of B–D. (G) Diagram representing the cell wall of *C. albicans* based on Lenardon *et al.* (2020).[65]

brane) layer is a matrix of glucans, proteins, and chitin[65,69] (which appears as a strong red colour in the combined image), corresponding to the additional amide contribution from the proteins in this region. Lastly, a thin blue line (between positions 1 & 2) can be observed corresponding to the phospholipids present in the cytoplasmic membrane, before moving into the cytoplasmic region of the fungal cell.

While the changes in the PiFM spectra of the yeast *C. albicans* were not particularly marked, this was not the case for the bacterium *E. coli* (Fig. 6A–D). Positions 1 & 4 were on the outer membrane of the bacterium, while positions 2 & 3 were towards the centre of the cell, close to the nucleoid and cytoplasm (Fig. 6E and F). The structure of the Gram-negative

bacterial cell envelope is well understood and consists of an inner (cytoplasmic) and outer membrane comprised of lipid bilayers, which encapsulate an intermembrane space (periplasm) containing a thin loosely cross-linked peptidoglycan layer.[70,71] The cell wall of Gram-negative bacteria is considerably thinner than that of Gram-positive species, with the peptidoglycan anchored to the outer membrane *via* murein lipoprotein, (LPP) which is the most abundant protein in *E. coli* cells.[72]

The outer membrane is composed of lipopolysaccharide (LPS) and phospholipids. The LPS layer is formed of a long polysaccharide chain (O antigen) which is embedded into the outer membrane *via* a phospholipid called lipid A.[73,74]
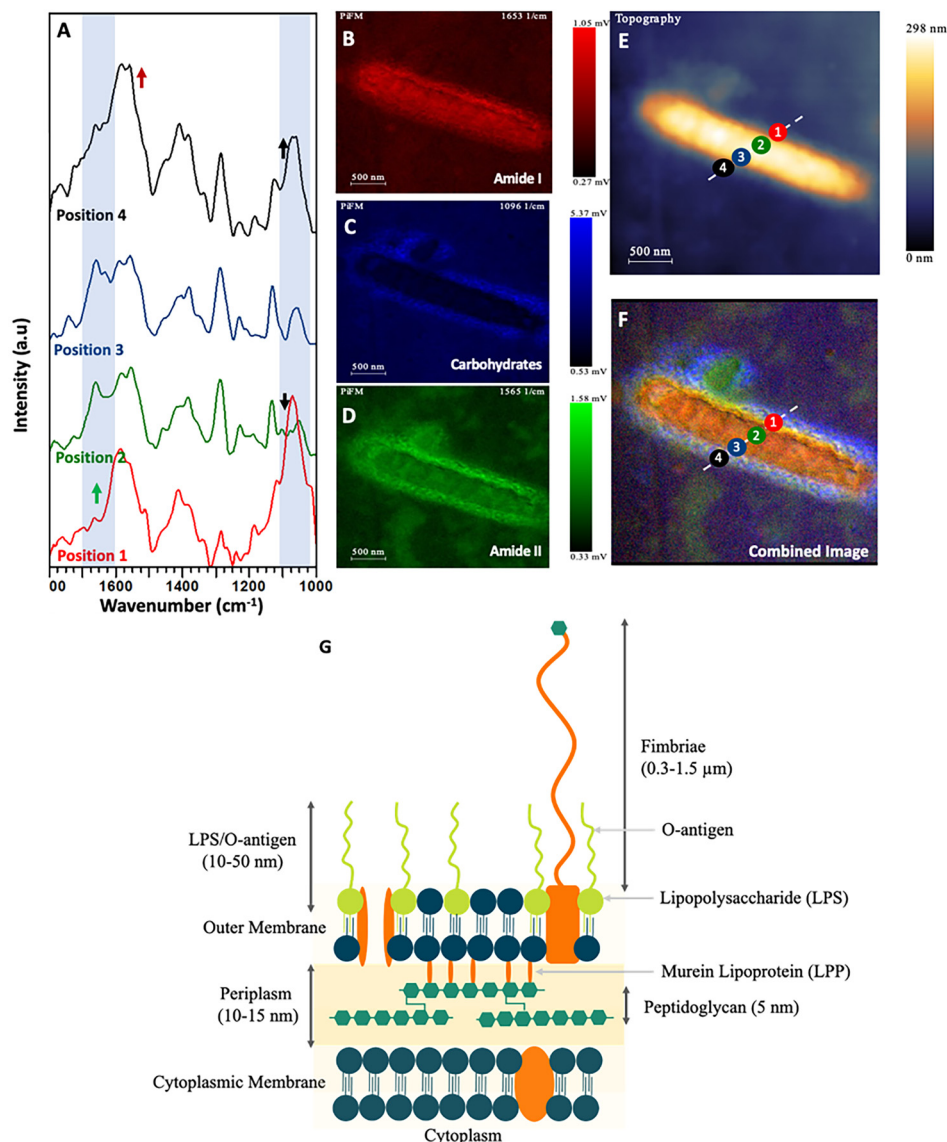
Fig. 6 (A) PiFM spectra taken from four positions (1 to 4) across a single *E. coli* cell section, where each position and colour correspond to the indicated position and colour in (E) and (F). (B) Spectral map of 1664 cm^{-1} intensity. (C) Spectral map of 1074 cm^{-1} intensity. (D) Spectral map of 1540 cm^{-1} intensity. (E) Topographical map of *E. coli* across the cell wall. (F) Combined image of B–D. (G) Diagram representing the cell wall of Gram-negative bacteria Clifton *et al.* (2013) and Pajerski *et al.* (2019).[66,67]

Consequently, the intense and broad peaks centred at approximately 1100 cm^{-1} and 1235 cm^{-1} may be ascribed to both the carbohydrate rich O antigen of LPS and P–O stretching in lipid A, as reported by Barkleit *et al.*[75] these areas being visualised as a blue halo in the outermost layer of the cell (Fig. 6). The PiFM spectra taken at positions 1 & 4 show intense peaks at both 1095 cm^{-1} and 1235 cm^{-1}, again in direct agreement with Barkleit *et al.*[75] There is an intensity contribution from amide I and amide II in this region, which is to be expected (and was also seen in the IR signal) and probably corresponds to outer membrane proteins. When comparing the intensities of the LPS to the amide I and II, it was found to only be localised around the outermost layer. As the peptidoglycan layer is closely associated with the outer membrane and is comprised

of complex carbohydrates[41] which absorb in similar areas to that of the LPS, (at 1105 and 1060 cm^{-1}), this signal probably contributes to the intensity observed in the 1095 cm^{-1} region (Fig. 6C). The inner part of the cell corresponds to the cytoplasm and nucleoid and was almost entirely devoid of any 1095 cm^{-1} intensity. Instead, this area was characterised by large contributions from amide I and amide II bands corresponding to the proteins and DNA present within the bacterium.

In contrast to Gram-negative bacteria, Gram-positive species such as *S. aureus* lack an outer membrane and do not produce LPS. Instead, the single (lipid-rich) cytoplasmic membrane is surrounded by a thick cell wall comprised of peptidoglycan and negatively charged teichoic acids (TA) to which it is
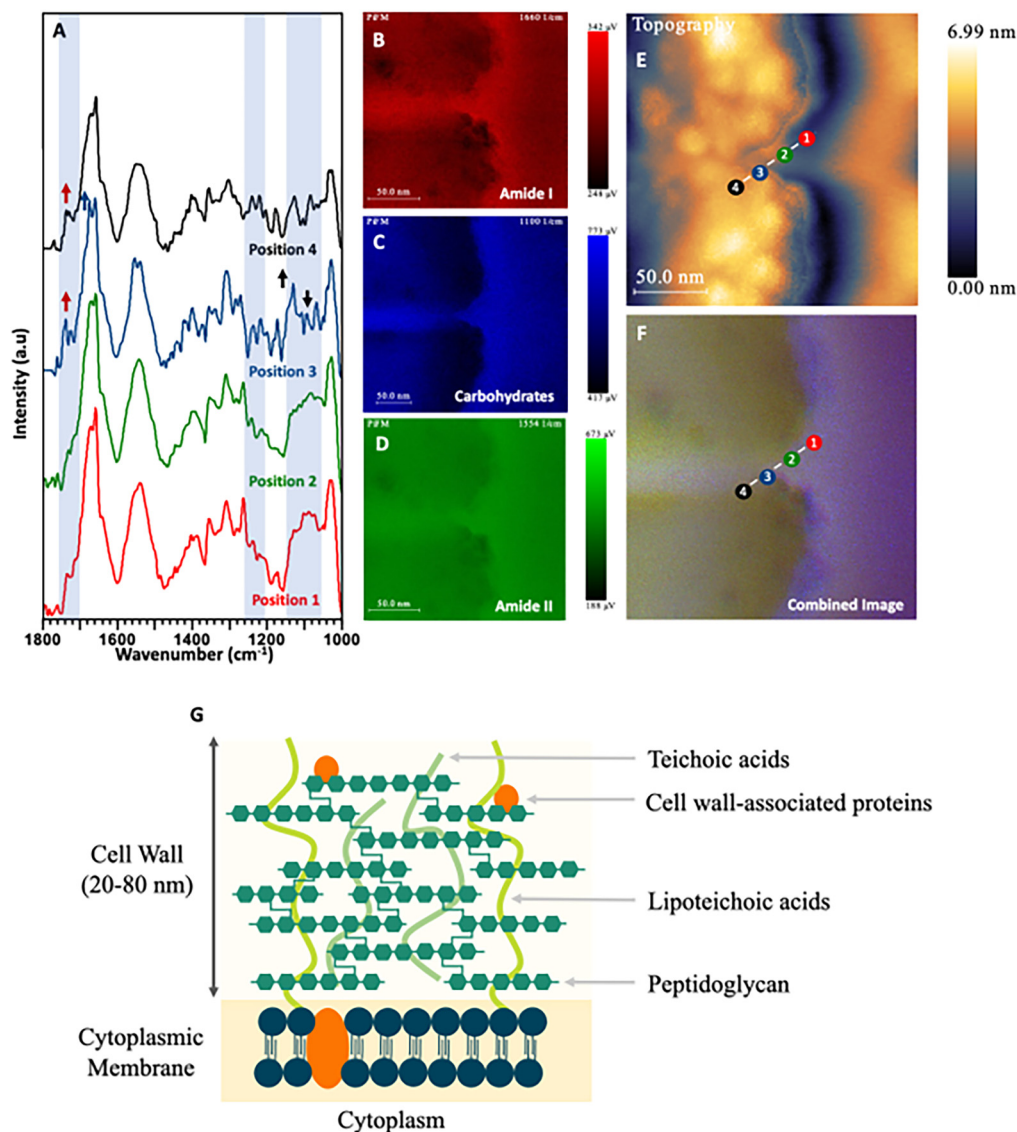
Fig. 7 (A) PiFM spectra taken from four positions (1 to 4) across the cell wall and cytoplasmic membrane of a *S. aureus* cell section where each position and colour corresponds to the indicated position and colour in (E) and (F). (B) Spectral map of 1664 cm^{-1} intensity. (C) Spectral map of 1074 cm^{-1} intensity. (D) Spectral map of 1540 cm^{-1} intensity. (E) Topographical map of *S. aureus* across the cell wall. (F) Combined image of B–D. (G) Diagram representing the cell wall of Gram-positive bacteria based on Lovering *et al*. (2010) and Pajerski *et al*. (2019).[67,68]

anchored (Fig. 7A–D). Positions 1 & 2 of the PiFM micrograph (Fig. 7E and F) sit upon this region, with the chemistry at these positions found to be very similar, with a broad peak between 1100–1050 cm^{-1} corresponding to the membrane phospholipids. In contrast to *E. coli*, however, a change in the intensity and full width half maxima of the polysaccharide areas was observed, which may be ascribed to the TA component of the cell wall (visible as a purple halo around the cell and along the septum between the dividing daughter cells). This layer is as distinct in the spectral map as in the topography image (Fig. 2C). The major difference in the transition between positions 1 & 2 and 3 & 4 is the emergence of a sharp peak at 1120 cm^{-1} and a shoulder at 1735 cm^{-1}; these being ascribable to glycogen and lipoproteins respectively. Although

positions 3 & 4 sit inside the cytoplasm of the *S. aureus* cell, they remain on the inner edge of the cytoplasmic membrane, which may explain the only slight variation in the spectra. The spectral imaging shows clearly that the inside of the bacteria is again mostly formed of amide I and amide II from the proteins and constituents of the cell within the cytoplasm.

This study successfully analysed Gram-positive, Gram-negative and yeast cells using PiFM, yielding high-resolution 3-dimensional topographical images and direct chemical mapping of specific points across the cell surface. Although bacterial peptidoglycan isolated from *Enterococcus faecium* has previously been analysed using PiFM (Wang *et al*. 2022), whole cell preparations as shown here have not been studied before.[76] Employing techniques that can visualise the struc-

tural biology of a cell can be used to aid our understanding of AMR, as well as having the potential to facilitate the development of new strategies to overcome it. Whilst this study investigated the structure of strains which were known to be susceptible to antibiotics, antimicrobials such as β-lactams, vancomycin, polymyxins and a number of antimicrobial peptides are known to target cell surface structures.[77,78] Using PiFM, treatment effects on these structures may now be potentially visualised and studied. Additionally, AMR to these antimicrobials could also similarly be studied, providing important, previously unseen insights into the biochemical and structural changes to the cell surface which may have arisen as a consequence of resistance. Only by more fully understanding AMR can we hope to combat its catastrophic effects.

Conclusion

This study demonstrates the powerful ability of PiFM to study the nanostructure of microbial samples directly, with applications as wide as colony formation behaviour and mechanisms of antimicrobial resistance. While TEM can provide higher resolution imaging, the molecular information provided by PiFM is particularly informative on the chemistry of the system. We have demonstrated that PiFM is able to precisely image the fine and complex biochemistry of cells, directly corroborating the findings of the established literature without the need for either labels or staining. We believe that this approach will become an important tool for the direct study of cell membranes, organelles, and artificial cell systems; the underlying biochemistry of which play key roles in cellular homeostasis, host–pathogen interactions, and susceptibility to antimicrobial agents.

Author contributions

JDJ – conceptualisation, methodology, validation, investigation, data curation, writing, funding acquisition. PRD – conceptualisation, supervision, writing – review and edit and funding acquisition. AG – writing review and methodology. DH – methodology and visualization. KH – supervision, writing – review and editing. MP – methodology, validation, and investigation

Conflicts of interest

There are no conflicts to declare.

Acknowledgements

References

1 K. Kochan, C. Nethercott, J. Taghavimoghaddam, Z. Richardson, E. Lai, S. A. Crawford, A. Y. Peleg, B. R. Wood and P. Heraud, *Anal. Chem.*, 2020, **92**, 8235–8243.

2 J. Zahller and P. S. Stewart, *Antimicrob. Agents Chemother.*, 2002, **46**, 2679.

3 A. Hisada, E. Matsumoto, R. Hirano, M. Konomi, J. Y. Bou Khalil, D. Raoult and Y. Ominami, *Sci. Rep.*, 2023, **13**, 11258.

4 T. Lithgow, C. J. Stubenrauch and M. P. H. Stumpf, *Nat. Rev. Microbiol.*, 2023, **21**, 502–518.

5 R. S. Brzozowski, M. L. White and P. J. Eswara, *J. Visualized Exp.*, 2019, 153.

6 C. L. M. Morais, K. M. G. Lima, M. Singh and F. L. Martin, *Nat. Protoc.*, 2020, **15**, 2143–2162.

7 S. Koide and S. S. Sidhu, *ACS Chem. Biol.*, 2009, **4**, 325.

8 N. K. Tonks, *Nat. Rev. Mol. Cell Biol.*, 2006, **7**, 833–846.

9 A. Martínez, J. Haavik, T. Flatmark, J. L. R. Arrondo and A. Muga, *J. Biol. Chem.*, 1996, **271**, 19737–19742.

10 Y. Wang, Y. Chang, L. Yin, Y. Xue, Z. Li and C. Xue, *Food Bioprocess Technol.*, 2016, **9**, 621–627.

11 S. A. Bhat and S. Ahmad, *J. Mol. Struct.*, 2016, **1105**, 169–177.

12 A. Barth, *Biochim. Biophys. Acta, Bioenerg.*, 2007, **1767**, 1073–1101.

13 D. Chapman, *J. Am. Oil Chem. Soc.*, 1965, **42**, 353–371.

14 E. Wiercigroch, E. Szafraniec, K. Czamara, M. Z. Pacia, K. Majzner, K. Kochan, A. Kaczor, M. Baranska and K. Malek, *Spectrochim. Acta, Part A*, 2017, **185**, 317–335.

15 D. Cozzolino, *Food Anal. Methods*, 2022, **15**, 1390–1396.

16 I. Pupeza, M. Huber, M. Trubetskov, W. Schweinberger, S. A. Hussain, C. Hofer, K. Fritsch, M. Poetzlberger, L. Vamos, E. Fill, T. Amotchkina, K. V. Kepesidis, A. Apolonski, N. Karpowicz, V. Pervak, O. Pronin, F. Fleischmann, A. Azzeer, M. Žigman and F. Krausz, *Nature*, 2020, **577**, 52–59.

17 C. R. Baiz, B. Błasiak, J. Bredenbeck, M. Cho, J. H. Choi, S. A. Corcelli, A. G. Dijkstra, C. J. Feng, S. Garrett-Roe, N. H. Ge, M. W. D. Hanson-Heine, J. D. Hirst, T. L. C. Jansen, K. Kwac, K. J. Kubarych, C. H. Londergan, H. Maekawa, M. Reppert, S. Saito, S. Roy, J. L. Skinner, G. Stock, J. E. Straub, M. C. Thielges, K. Tominaga, A. Tokmakoff, H. Torii, L. Wang, L. J. Webb and M. T. Zanni, *Chem. Rev.*, 2020, **120**, 7152–7218.

18 Y. Phal, L. Pfister, P. S. Carney and R. Bhargava, *J. Phys. Chem. C*, 2022, **126**, 9777–9783.

19 E. Abbe, *Arch. Mikrosk. Anat.*, 1873, **9**, 413–418.

20 P. Lasch and D. Naumann, *Biochim. Biophys. Acta, Biomembr.*, 2006, **1758**, 814–829.

21 M. Krieg, G. Fläschner, D. Alsteens, B. M. Gaub, W. H. Roos, G. J. L. Wuite, H. E. Gaub, C. Gerber, Y. F. Dufrêne and D. J. Müller, *Nat. Rev. Phys.*, 2019, **1**, 41–57.

22 K. Umeda, S. J. Mcarthur and N. Kodera, *Microscopy*, 2023, **72**, 151–161.

23 A. Miranda, A. I. Gómez-Varela, A. Stylianou, L. M. Hirvonen, H. Sánchez and P. A. A. De Beule, *Nanoscale*, 2021, **13**, 2082–2099.

24 J. A. Davies-Jones and P. R. Davies, *Mater. Chem. Front.*, 2022, **6**, 1552–1573.

25 L. M. Otter, M. W. Förster, E. Belousova, P. O'Reilly, D. Nowak, S. Park, S. Clark, S. F. Foley and D. E. Jacob, *Geostand. Geoanal. Res.*, 2021, **45**, 5–27.

26 A. M. Joshua, G. Cheng and E. V. Lau, *Appl. Surf. Sci. Adv.*, 2023, **17**, 100448.

27 G. M. McClelland, R. Erlandsson and S. Chiang, *Rev. Prog. Quant. Nondestr. Eval.*, 1987, 1307–1314.

28 R. Garcia and R. Proksch, *Eur. Polym. J.*, 2013, **49**, 1897–1906.

29 M. A. Almajhadi, S. M. A. Uddin and H. K. Wickramasinghe, *Nat. Commun.*, 2020, **11**, 5691.

30 D. Nowak, W. Morrison, H. K. Wickramasinghe, J. Jahng, E. Potma, L. Wan, R. Ruiz, T. R. Albrecht, K. Schmidt, J. Frommer, D. P. Sanders and S. Park, *Sci. Adv.*, 2016, **2**, e1501571.

31 A. A. Sifat, J. Jahng and E. O. Potma, *Chem. Soc. Rev.*, 2022, **51**, 4208–4222.

32 J. Mathurin, A. Deniset-Besseau, D. Bazin, E. Dartois, M. Wagner and A. Dazzi, *J. Appl. Phys.*, 2022, **131**, 10901.

33 D. V. Kazantsev, E. V. Kuznetsov, S. V. Timofeev, A. V. Shelaev and E. A. Kazantseva, *Phys.-Usp.*, 2017, **60**, 259.

34 M. Moo-Young, *Comprehensive Biotechnology*, 2019, ch. 1.41, pp. 561–571.

35 A. Lewis, A. Radko, N. Ben Ami, D. Palanker and K. Lieberman, *Trends Cell Biol.*, 1999, **9**, 70–73.

36 A. Rygula, T. Oleszkiewicz, E. Grzebelus, M. Z. Pacia, M. Baranska and R. Baranski, *Spectrochim. Acta, Part A*, 2018, **197**, 47–55.

37 J. Wang, L. Peng, D. Han, T. Zheng, T. Chang and H. L. Cui, *Front. Microbiol.*, 2023, **14**, 1195448.

38 S. Gamage, M. Howard, H. Makita, B. Cross, G. Hastings, M. Luo and Y. Abate, *PLoS One*, 2018, **13**, e0199112.

39 Q. Zhu, R. Zhou, J. Liu, J. Sun and Q. Wang, *Nanomaterials*, 2021, **11**, 1353.

40 K. Kochan, C. Nethercott, D. Perez-Guaita, J. H. Jiang, A. Y. Peleg, B. R. Wood and P. Heraud, *Anal. Chem.*, 2019, **91**, 15397–15403.

41 K. Kochan, D. Perez-Guaita, J. Pissang, J. H. Jiang, A. Y. Peleg, D. McNaughton, P. Heraud and B. R. Wood, *J. R. Soc., Interface*, 2018, **15**, 20180115.

42 A. P. Fellows, M. T. L. Casford and P. B. Davies, *J. Microsc.*, 2021, **284**, 189–202.

43 N. Matsko and M. Mueller, *J. Struct. Biol.*, 2004, **146**, 334–343.

44 N. Fairley, *CasaXPS Manual: 2.3.15 Spectroscopy*, 2009.

45 L. M. Otter, K. Eder, M. R. Kilburn, L. Yang, P. O'Reilly, D. B. Nowak, J. M. Cairney and D. E. Jacob, *Nat. Commun.*, 2023, **14**, 2254.

46 M. Suleiman, G. Abu-Aqil, U. Sharaha, K. Riesenberg, O. Sagi, I. Lapidot, M. Huleihel and A. Salman, *Analyst*, 2021, **146**, 1421–1429.

47 G. Abu-Aqil, M. Suleiman, U. Sharaha, L. Nesher, I. Lapidot, A. Salman and M. Huleihel, *Spectrochim. Acta, Part A*, 2023, **295**, 122634.

48 U. Sharaha, M. Suleiman, G. Abu-Aqil, K. Riesenberg, I. Lapidot, A. Salman and M. Huleihel, *Anal. Chem.*, 2021, **93**, 13426–13433.

49 U. Sharaha, G. Abu-Aqil, M. Suleiman, K. Riesenberg, I. Lapidot, M. Huleihel and A. Salman, *J. Biophotonics*, 2023, **16**, e202200198.

50 M. J. Fiołka, S. Mieszawska, P. Czaplewska, A. Szymańska, K. Stępnik, W. Sofińska-Chmiel, T. Buchwald and K. Lewtak, *Sci. Rep.*, 2020, **10**, 16352.

51 A. Dazzi, R. Prazeres, F. Glotin and J. M. Ortega, *Infrared Phys. Technol.*, 2006, **49**, 113–121.

52 S. Wongthong, P. Tippayawat, M. Wongwattanakul, P. Poung-ngern, L. Wonglakorn, A. Chanawong, P. Heraud and A. Lulitanond, *World J. Microbiol. Biotechnol.*, 2020, **36**, 1–12.

53 B. Feng, H. Shen, F. Yang, J. Yan, S. Yang, N. Gan, H. Shi, S. Yu and L. Wang, *Spectrochim. Acta, Part A*, 2022, **279**, 121369.

54 H. Lamprell, G. Mazerolles, A. Kodjo, J. F. Chamba, Y. Noël and E. Beuvier, *Int. J. Food Microbiol.*, 2006, **108**, 125–129.

55 A. Muller and J. Grazul, *J. Electron Microsc.*, 2001, **50**, 219–226.

56 Q. Lv, L. Yan and Y. Jiang, *Front. Microbiol.*, 2021, **12**, 3774.

57 T. Tsuji and T. Fujimoto, *Biochem. Soc. Trans.*, 2018, **46**, 1047–1054.

58 S. C. Li and P. M. Kane, *Biochim. Biophys. Acta, Mol. Cell Res.*, 2009, **1793**, 650–663.

59 J. Suchodolski, J. Muraszko, P. Bernat and A. Krasowska, *Microorganisms*, 2019, **7**, 378.

60 V. Cabezón, A. Llama-Palacios, C. Nombela, L. Monteoliva and C. Gil, *Proteomics*, 2009, **9**, 4770–4786.

61 J. Lever, M. Krzywinski and N. Altman, *Nat. Methods*, 2017, **14**, 641–642.

62 A. N. Spitsyn, D. V. Utkin, O. S. Kuznetsov, P. S. Erokhin, N. A. Osina and V. I. Kochubei, *Opt. Spectrosc.*, 2021, **129**, 135–148.

63 D. Alexandrakis, G. Downey and A. G. M. Scannell, *J. Agric. Food Chem.*, 2008, **56**, 3431–3437.

64 R. Garcia-Rubio, H. C. de Oliveira, J. Rivera and N. Trevijano-Contador, *Front. Microbiol.*, 2020, **10**, 2993.

65 M. D. Lenardon, P. Sood, H. C. Dorfmueller, A. J. P. Brown and N. A. R. Gow, *Cell Surf.*, 2020, **6**, 100047.

66 L. A. Clifton, M. W. A. Skoda, E. L. Daulton, A. V. Hughes, A. P. Le Brun, J. H. Lakey and S. A. Holt, *J. R. Soc., Interface*, 2013, **10**, 20130810.

67 W. Pajerski, D. Ochonska, M. Brzychczy-Wloch, P. Indyka, M. Jarosz, M. Golda-Cepa, Z. Sojka and A. Kotarba, *J. Nanopart. Res.*, 2019, **21**, 1–12.

68 A. L. Lovering, L. Y. C. Lin, E. W. Sewell, T. Spreter, E. D. Brown and N. C. J. Strynadka, *Nat. Struct. Mol. Biol.*, 2010, **17**, 582–589.

69 A. Cassone, *Nat. Rev. Microbiol.*, 2013, **11**, 884–891.

70 M. Mathelié-Guinlet, A. T. Asmar, J. F. Collet and Y. F. Dufrêne, *Nat. Commun.*, 2020, **11**, 1789.

71 T. J. Silhavy, N. Ruiz and D. Kahne, *Nat. Rev. Microbiol.*, 2006, **4**, 57–66.

72 T. J. Silhavy, D. Kahne and S. Walker, *Cold Spring Harbor Perspect. Biol.*, 2010, **2**, a000414.

73 A. Steimle, I. B. Autenrieth and J. S. Frick, *Int. J. Med. Microbiol.*, 2016, **306**, 290–301.

74 J. L. Ding and B. Ho, *Subcell. Biochem.*, 2010, **53**, 187–208.

75 A. Barkleit, H. Foerstendorf, B. Li, A. Rossberg, H. Moll and G. Bernharda, *Dalton Transactions*, 2011, **40**, 9868–9876.

76 H. Wang, Q. Xie and X. G. Xu, *Adv. Drug Delivery Rev.*, 2022, **180**, 114080.

77 A. Farkas, G. Maróti, A. Kereszt and É. Kondorosi, *Front. Microbiol.*, 2017, **8**, 241211.

78 M. F. Chellat, L. Raguž and R. Riedl, *Angew. Chem., Int. Ed.*, 2016, **55**, 6600–6626.